

# **Description of a rigorous procedure to evaluate the antenna temperature and its application to BEST-1<sup>1</sup>**

Pietro Bolli, Federico Perini, Stelio Montebugnoli, Giuseppe Pelosi\*

\* Dipartimento di Elettronica e Telecomunicazioni, Università di Firenze, I-50134 Florence, Italy

IRA Technical Report N° 377/05

---

<sup>1</sup> This study has been developed in order to prepare the italian contribution for the white paper on the antenna sub-systems for the SKA project: P.D. Patel, “Antenna Concepts Consideration for SKA”, October 2005

## INDEX

1. ABSTRACT.....	3
2. ANTENNA TEMPERATURE .....	3
3. BRIGHTNESS TEMPERATURE.....	7
4. ALGORITHM DESCRIPTION.....	16
5. BEST-1 DESCRIPTION.....	18
6. BEST-1 ELECTROMAGNETIC ANALYSIS & ANTENNA TEMPERATURE CALCULATION .....	19
7. ACKNOWLEDGMENT.....	30
8. REFERENCES.....	31
APPENDIX A .....	33

## 1. ABSTRACT

This technical report describes a rigorous procedure for antenna temperature calculation which, usually, is just estimated and/or approximated experimentally. To comply with this task both brightness temperature distribution and antenna pattern are required as input data. In order to compute the antenna temperature, a proprietary code (both in Fortran and in Matlab language) has been developed and applied to several different cases. The brightness temperature is also evaluated via the same proprietary code by using the formulas described in this report. The antenna pattern computation however, is demanded to an external tool: several different software capable to evaluate the 3D antenna pattern could be used, among them in this report we have chosen the commercial software GRASP developed by TICRA. Despite the here followed procedure has general validity and, as such, applicable to every kind of antenna, the numerical results presented in this report have been obtained for BEST-1 (Basic Element for SKA Training), which represents a SKA (Square Kilometer Array, <http://www.skatelescope.org/>) demonstrator based on cylindrical parabolic antennas.

## 2. ANTENNA TEMPERATURE

As well known, among the many parameters which characterize the antenna performance, one of the most important is the antenna temperature, especially in radio astronomy where signals to be received might even be 60dB below receiver noise. The evaluation of this parameter requires the knowledge of both the antenna pattern and the brightness temperature distribution in the whole space surrounding the antenna itself. According to [1], a very general formula to define the antenna noise temperature at the frequency  $\nu$  is given by:

$$T_{ant}(\nu; \Theta_0, \Phi_0, \Delta_0) = \frac{\iint_{\substack{\theta=0,\pi \\ \phi=0,2\pi}} P_n(\nu; \theta, \phi) T_b(\nu; \theta', \phi') \sin \theta d\theta d\phi}{\iint_{\substack{\theta=0,\pi \\ \phi=0,2\pi}} P_n(\nu; \theta, \phi) \sin \theta d\theta d\phi} \quad (1)$$

where:

$$\begin{aligned}\theta' &= \theta'(\theta, \phi, \Theta_0, \Phi_0, \Delta_0) \\ \phi' &= \phi'(\theta, \phi, \Theta_0, \Phi_0, \Delta_0)\end{aligned}\tag{2}$$

and  $(\Theta_0, \Phi_0, \Delta_0)$  are the antenna pointing directions:  $\Theta_0$  is the co-elevation angle,  $\Phi_0$  is the azimuth angle of the antenna axis and  $\Delta_0$  is the rotation angle of the antenna system around its main axis. The rotation is carried out as explained in the appendix of [1]. In Fig.1, a sketch of the relation between the antenna radiation pattern and the brightness temperature is shown.

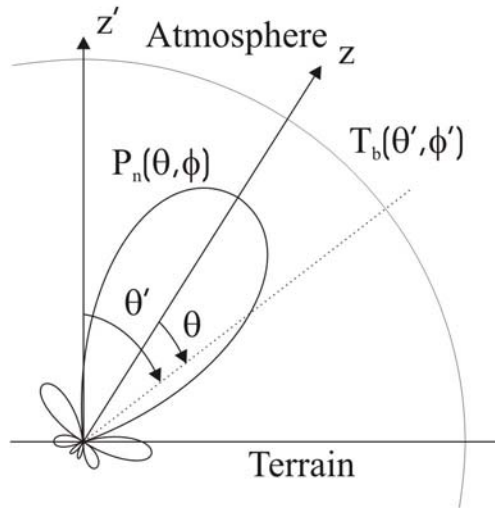


**Figure 1** – Scenario of the space surrounding the antenna.

Moreover, in (1)  $P_n(\nu; \theta, \phi)$  is the total (Co-polar + Cross-polar) radiation antenna power pattern and  $T_b(\nu; \theta', \phi')$  is the brightness temperature distribution. As one can see from (1), these parameters are given as a function of two different reference systems: antenna pattern is given in the reference system of the antenna pointing direction (called x-y-z), whereas the brightness temperature is in that of the earth (called x'-y'-z'), therefore z' coincides with the local zenith direction. In order to compute the integral, they have to be transformed in the same reference

system. In particular, according to [1], we have chosen to transform the brightness temperature into the antenna reference system. Since the two systems have the same origin, three angles are sufficient to transform one system into another. Hence, the functions introduced in [1] are used to convert the variables:

$$\begin{aligned} \theta' &= \arccos \left[ \sin \Theta_0 \sin \theta \sin(\phi + \Delta_0) + \cos \Theta_0 \cos \theta \right] \\ \phi' &= \arctan \left[ \frac{\sin \Phi_0 \sin \theta \sin(\phi + \Delta_0) + \cos \Phi_0 \cos \Theta_0 \sin \theta \sin(\phi + \Delta_0) - \cos \Phi_0 \sin \Theta_0 \cos \theta}{\cos \Phi_0 \sin \theta \cos(\phi + \Delta_0) - \sin \Phi_0 \cos \Theta_0 \sin \theta \sin(\phi + \Delta_0) + \sin \Phi_0 \sin \Theta_0 \cos \theta} \right] \end{aligned} \quad (3)$$

In this way, it is possible to find  $\theta', \phi'$  for every  $\theta, \phi$ , given the position of the antenna axis in terms of  $(\Theta_0, \Phi_0, \Delta_0)$ . It is worth to notice that, since the brightness temperature distribution could be assumed rotation symmetrical,  $T_b(\nu; \theta')$  can be used instead of  $T_b(\nu; \theta', \phi')$ . For this reason, generally, the  $\phi'$  angle is not calculated; however, this is not true in our case, where it is necessary to transform also the direction of the antenna pattern components, as it is shown in the last part of this section of the paper.

A simpler (but erroneous) way to compute  $\theta'$  is with the expression (see again [1]):

$$\theta' = \theta - \Theta_0 \quad (4)$$

where the spherical coordinate is written as a shift in the  $(\theta, \phi)$  plane. For example, for a particular case with  $\Theta_0 = 30^\circ$ ,  $\Delta_0 = 0^\circ$  and  $\theta = 60^\circ$ , a plot of the value of  $\theta'$ , both as described in (3) and in (4), versus  $\phi$  is shown in Fig.2. As a matter of fact, from Fig.2, it is evident that using (4) in place of (3) means to have values of  $\theta'$  smaller (as well known, brightness temperature increases with  $\theta'$ ), yielding an underestimation of the antenna temperature.

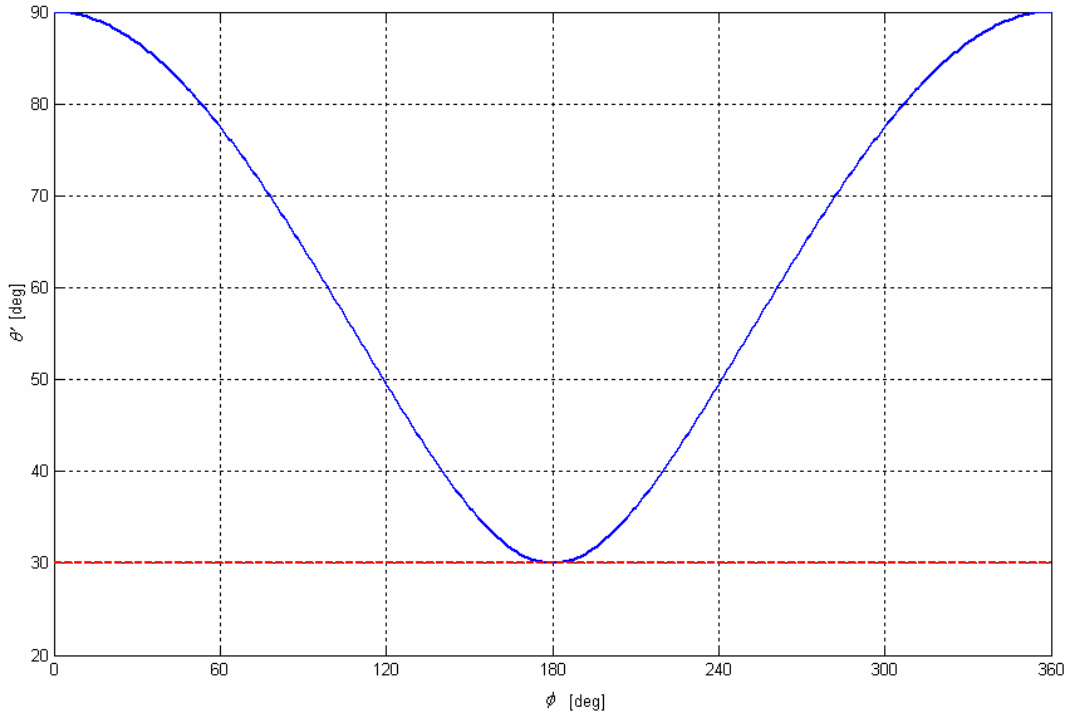


**Figure 2** – Behavior of  $\theta'$  against  $\phi$ . The blue line represents (3), whereas the dashed red line (4).

A slightly complication needs to be introduced now, it derives from the fact that ground emission and scattering is a polarization dependent process (see [2]). In fact, as explained in more detail in the next section, the antenna pattern has to be described with respect to the directions relative to the plane of incidence, right at the surface interaction, represented by the plane  $z'=0$  (i.e.  $\theta' = 90^\circ$ ). In the problem under exam, we have that the two directions parallel and perpendicular to the plane of incidence ( $\hat{u}_{\parallel}, \hat{u}_{\perp}$ ) are respectively:  $\hat{\theta}', \hat{\phi}'$ . Hence, the far field antenna pattern has to be transformed from the components along the antenna reference system ( $P_{\theta}, P_{\phi}$ ) to the ones in the earth reference system ( $P_{\theta'}, P_{\phi'}$ ). In order to perform this transformation, three different steps are introduced:  $\hat{\rho}, \hat{\theta}, \hat{\phi} \rightarrow \hat{x}, \hat{y}, \hat{z} \rightarrow \hat{x}', \hat{y}', \hat{z}' \rightarrow \hat{\rho}', \hat{\theta}', \hat{\phi}'$ . This transformation yields a multiplication among several matrices:

$$\begin{bmatrix} 0 \\ P_{\theta'} \\ P_{\phi'} \end{bmatrix} = \underline{[A]}_{\hat{x}', \hat{y}', \hat{z}' \rightarrow \hat{\rho}', \hat{\theta}', \hat{\phi}'} \underline{[B]}_{\hat{x}, \hat{y}, \hat{z} \rightarrow \hat{x}', \hat{y}', \hat{z}'} \underline{[C]}_{\hat{\rho}, \hat{\theta}, \hat{\phi} \rightarrow \hat{x}, \hat{y}, \hat{z}} \begin{bmatrix} 0 \\ P_{\theta} \\ P_{\phi} \end{bmatrix} \quad (5)$$

where:

$$\underline{\underline{[A]}}_{\hat{x}', \hat{y}', \hat{z}' \rightarrow \hat{\rho}', \hat{\theta}', \hat{\phi}'} = \begin{bmatrix} \sin \theta' \cos \phi' & \sin \theta' \sin \phi' & \cos \theta' \\ \cos \theta' \cos \phi' & \cos \theta' \sin \phi' & -\sin \theta' \\ -\sin \phi' & \cos \phi' & 0 \end{bmatrix} \quad (6)$$

$$\underline{\underline{[B]}}_{\hat{x}, \hat{y}, \hat{z} \rightarrow \hat{x}', \hat{y}', \hat{z}'} = \begin{bmatrix} \cos \Phi_0 \cos \Delta_0 - & -\cos \Phi_0 \sin \Delta_0 - & \sin \Phi_0 \sin \Theta_0 \\ -\sin \Phi_0 \cos \Theta_0 \sin \Delta_0 & -\sin \Phi_0 \cos \Theta_0 \cos \Delta_0 & \\ \sin \Phi_0 \cos \Delta_0 + & -\sin \Phi_0 \sin \Delta_0 + & -\cos \Phi_0 \sin \Theta_0 \\ +\cos \Phi_0 \cos \Theta_0 \sin \Delta_0 & +\cos \Phi_0 \cos \Theta_0 \cos \Delta_0 & \\ \sin \Theta_0 \sin \Delta_0 & \sin \Theta_0 \cos \Delta_0 & \cos \Theta_0 \end{bmatrix} \quad (7)$$

$$\underline{\underline{[C]}}_{\hat{\rho}, \hat{\theta}, \hat{\phi} \rightarrow \hat{x}, \hat{y}, \hat{z}} = \begin{bmatrix} \sin \theta \cos \phi & \cos \theta \cos \phi & -\sin \phi \\ \sin \theta \sin \phi & \cos \theta \sin \phi & \cos \phi \\ \cos \theta & -\sin \theta & 0 \end{bmatrix} \quad (8)$$

Concluding,  $\underline{\underline{[B]}}_{\hat{x}, \hat{y}, \hat{z} \rightarrow \hat{x}', \hat{y}', \hat{z}'}$  is defined in [1] and allows the transformation of two rectangular coordinate systems, whereas the other two matrices perform the transformation from rectangular to spherical (and vice-versa) components.

### 3. BRIGHTNESS TEMPERATURE

As just anticipated in section 2, to calculate the antenna temperature, according to (1), it is necessary to know the brightness temperature distribution of the entire scene (on all the solid angle) that surrounds the antenna, or in other words, the “world” seen by the antenna through its power pattern. The brightness temperature distribution of the entire scene can be subdivided in two main contributions: from the sky range ( $0^\circ \leq \theta' \leq 90^\circ$ ) and from the ground range ( $90^\circ < \theta' \leq 180^\circ$ ). The first term is the radiation coming directly form the sky (this is discussed in the first part of this

section), whereas the latter is due to the sky radiation reflected from the ground and the emission from the ground itself.

A general expression for the sky brightness temperature measured from the ground can be:

$$T_b^{sky}(\nu; \theta') = T_{bo}(\nu) e^{-\tau_\nu(0, \infty)} + \int_0^\infty k_a(\nu; z') T_{atm}(z') e^{-\tau_\nu(0, z')} dz' \quad (9)$$

where  $T_{bo}(\nu)$  is the background brightness temperature due to cosmic emission,  $T_{atm}(z')$  and  $k_a(\nu; z')$  are, respectively, the physical temperature and the absorption coefficient of the atmosphere at the specified height above ground,  $z'$ , and:

$$\tau_\nu(0, \infty) = \int_0^\infty k_a(\nu; z') dz' \quad (10)$$

is the zenith opacity, that is the atmosphere opacity on a vertical path ( $\theta' = 0$ ). In (9) and (10) the superior limit of the integral is  $\infty$  to indicate that the integral is evaluated on the overall atmosphere's thickness, which is not well defined. There is an implicit dependence of  $T_b^{sky}$  from the zenith angle  $\theta'$ , because the optical path in the atmosphere depends to its incident angle.

To describe the sky brightness temperature (i.e. the emission from the gases in the atmosphere, the apparent temperature of the sky background seen through the atmosphere and the emission and scattering from the ground) several models are available in literature. Here we use the models collected and proposed in [2], because those ones were selected as guideline by the Antenna Task Force (ATF), part of the Engineering Working Group (EWG) of the SKA world consortium. In particular the models here adopted are for the water-vapor and oxygen absorption coefficients,  $k_a(\nu; z') = k_{H_2O}(\nu; z') + k_{O_2}(\nu; z')$ , and for the background cosmic emission term. For the last one, some considerations are necessary. The expression adopted is:

$$T_{bo}(\nu) = T_{CMB} + T_{g_o}(\nu_0/\nu)^\beta \quad (11)$$

where the first term,  $T_{CMB} = 2.73$  K, is the cosmic microwave background emission, and the second one is the galactic emission. The galactic emission depends directly to the frequency and indirectly to the observed direction in the sky, through the base temperature  $T_{g_o}$  and the spectral index  $\beta$ . For example:  $T_{g_o}$  varies from a minimum of 3K to a maximum of 507K, the latter in the direction of the galactic center, and with a value of 18K at the galactic poles. At the same time,  $\beta$  varies from 2.5 at in the direction of the galactic center to 3.2 within a small region just above the galactic plane. Moreover the average value of  $\beta$  is slowly varying with frequency and so, by adopting an average value of  $\beta = 2.75$ , with  $T_{g_o} = 20$  K at  $\nu_o = 0.408$  GHz, it is possible to obtain very reasonable results for galactic contributions to the antenna noise calculations for frequency  $\nu \geq 0.01$  GHz [2,3,4].

Starting from (9) and (10) and considering the successive Fig.3, it is possible to write the final expression of the sky brightness temperature distribution, where the dependence from  $\theta'$  is now explicit:

$$T_b^{sky}(\nu; \theta') = T_{bo}(\nu) e^{-\tau_{v,\theta'}(0, h_a)} + \int_0^{h_a} \frac{k_a(\nu; z') T_{am}(z') e^{-\tau_{v,\theta'}(0, z')}}{\sqrt{1 - (\sin(\theta')/(1 + (z'/r_e)))^2}} dz' \quad (12)$$

$$\tau_{v,\theta'}(0, h_a) = \int_0^{h_a} \frac{k_a(\nu; z')}{\sqrt{1 - (\sin(\theta')/(1 + (z'/r_e)))^2}} dz' \quad (13)$$

where  $r_e$  is the earth radius, the other symbols have the same meaning as in previous expressions. In (12) and (13) a finite value of the superior limit of integration ( $h_a$  instead  $\infty$ ) is considered, in other words we model the atmosphere as a layer, beginning on the earth surface, with a well defined thickness  $h_a$ . The square roots in the above expressions are extension factors of the atmospheric optical paths, for pointing not at the zenith ( $\theta' \neq 0^\circ$ ), that considers also the effect of the finite curvature of the earth surface [5].

The integrals represent the optical depth, or medium opacity, where the electromagnetic radiation is propagating. The integration domain, for each value of  $\theta'$ , corresponds to the optical path, the blue arrow in the Fig.3, through the atmosphere to the antenna.

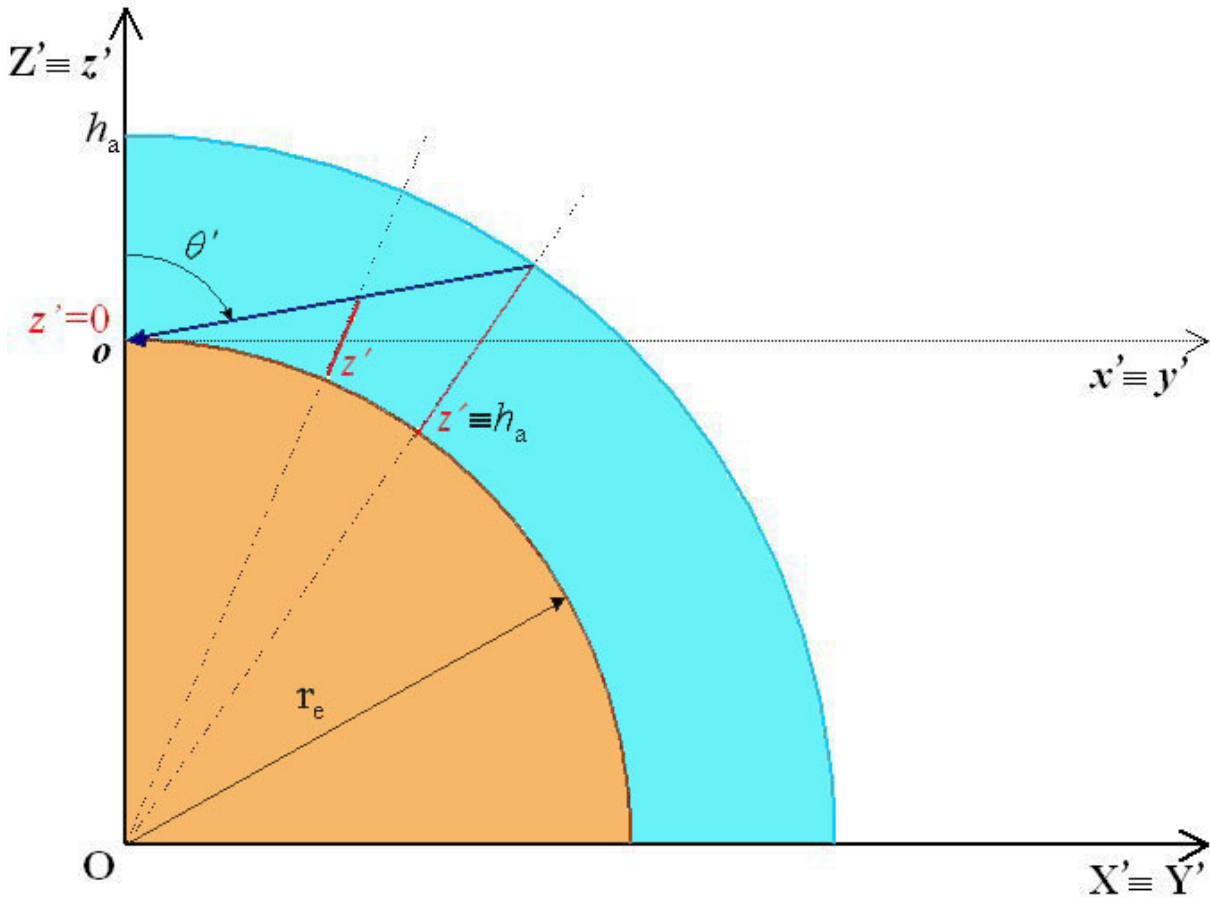


**Figure 3** – Sketch of the atmosphere-earth surface scenario used for the numerical integration of the atmosphere opacity. The antenna is located in the origin of the  $x'y'z'$  coordinate reference system,  $r_e$  and  $h_a$  are, respectively, the earth radius and the maximum atmosphere height.

A Matlab script to calculate all the terms included in the expression (12) and (13) has been developed. To solve the integrals, since it is not possible write their arguments in a simple analytic form, we can not use the Matlab symbolic integration tool, that doesn't require the explicit discretization of the integral domain, but only a more approximate function based on the trapezoidal method [6,7].

To calculate the atmospheric attenuation due to gasses' absorption along a vertical path, it is sufficient modeling the atmosphere as a planar multilayer with uniform thickness of 1Km and then sum up the respective contributions [8]. We verified that to obtain a good level of accuracy, for zenith angles between  $80^\circ$  and  $90^\circ$ , it would be necessary to decrease too much the 1Km step, but the calculation algorithm becomes too heavy. Moreover an uniform stratification doesn't take into account that farther from the earth surface the atmospheric layers are, less significant they become. To obtain a good compromise between accuracy and computation time, we have chosen to discretize the interval  $0 \leq h \equiv z' \leq h_a$ , with a logarithmic distribution of 501 points from the sea level to 100Km (from  $10^{-6}$  to  $10^2$  Km). The value  $h_a = 100$  Km is proposed in [2]. In the logarithmic distribution, the step  $\Delta h \equiv \Delta z'$  is not uniform, but is increasing with the value of width  $h_i \equiv z'_i$  (see Fig.4 and Fig.5)

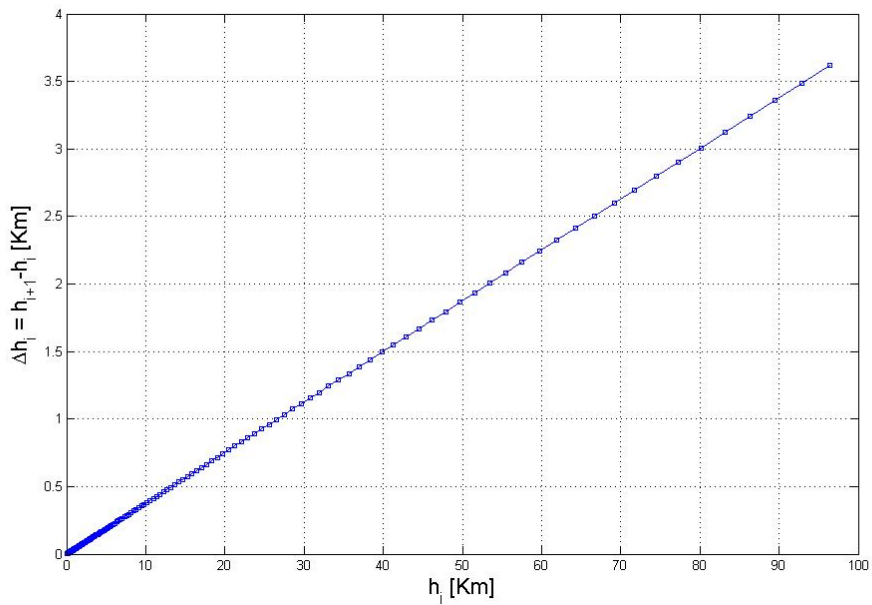


**Figure 4** –Incremental step altitude distribution.

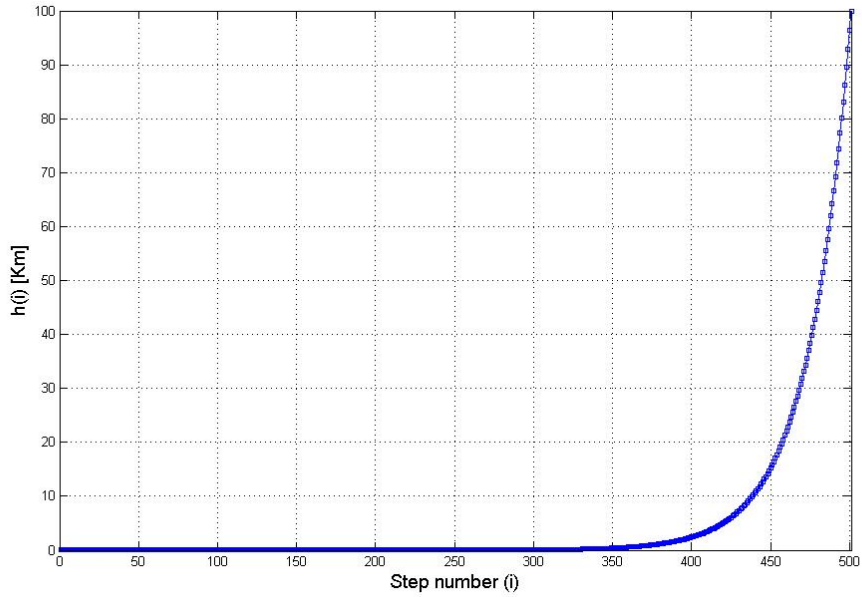


**Figure 5** – Atmospheric layers altitude distribution.

The sky brightness temperature up to 100GHz was calculated at different zenith angles and at different parameters for the cosmic emission (see Fig.6). The intermediate traces' group is under the same conditions of [2]:  $\beta = 2.75$ ,  $T_{g_o} = 20$  K and  $h_a = 100$  Km. The others two groups, the lower one and the higher one, are to intend as limit cases for the background cosmic emission. In particular, the lower group is referred at the direction of the galactic center ( $\beta = 2.5$  and  $T_{g_o} = 507$  K), while the lower group is referred at one cold sky region ( $T_{g_o} = 3$  K), with a high spectral index ( $\beta = 3.2$ ).

The results are reported also in a table format (see Appendix 1). Using the table, where only the intermediate group is collected, one can check the good agreement between our calculated values and those of [2].

How it is possible to deduce from Fig.6, the sky brightness temperature is strongly function of the  $T_{g_o}$ , which depends from the pointing direction in the sky, especially for frequency below 1GHz. For this reason, antenna temperature calculation for antenna operating in this range requires particular care in the  $\beta$  and  $T_{g_o}$  values selection.

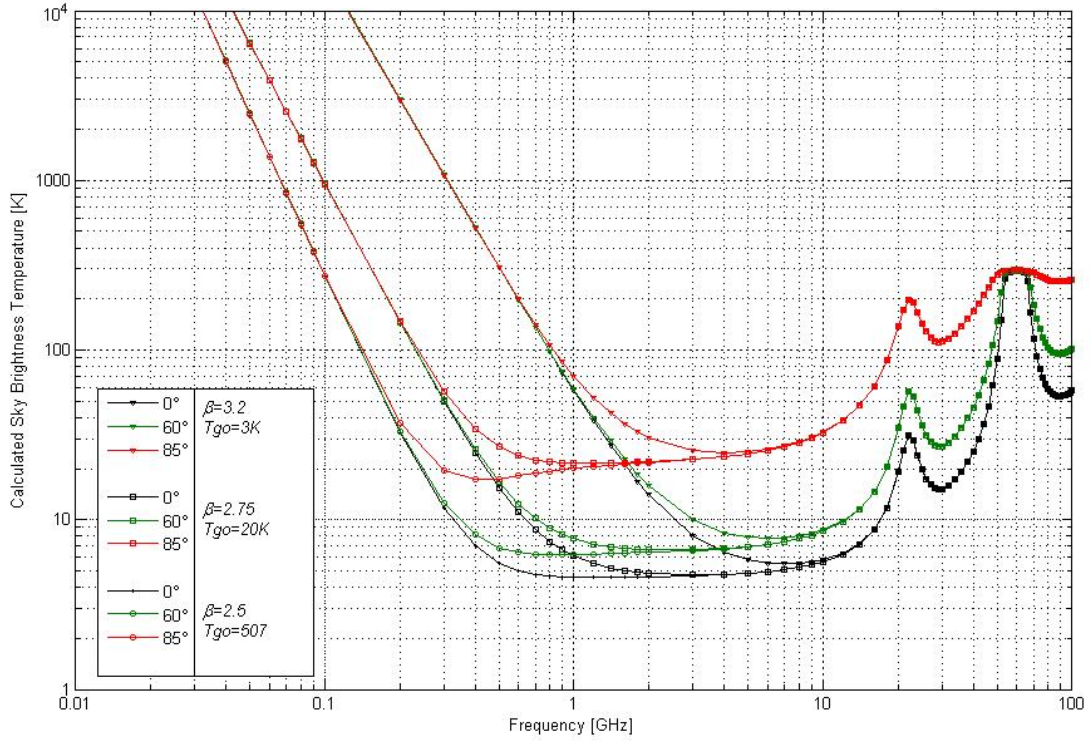


**Figure 6** - Calculated Sky Brightness Temperature as a function of frequency obtained by numerically integrating of (12).

Now we consider the second contribution at the brightness temperature distribution: the emission and scattering from the ground. For this reason we rewrite the argument of the integral in (1) as [2]:

$$P_n(\nu; \theta, \phi) T_b(\nu; \theta') = \begin{cases} T_b^{sky}(\nu; \theta') P_n(\nu; \theta, \phi) & 0^\circ \leq \theta' \leq 90^\circ \\ T_{b\parallel}(\nu; \theta') P_{\parallel}(\nu; \theta, \phi) + T_{b\perp}(\nu; \theta') P_{\perp}(\nu; \theta, \phi) & 90^\circ < \theta' \leq 180^\circ \end{cases} \quad (14)$$

$$\begin{aligned} T_{b\parallel}(\nu; \theta') &= T_{\parallel}^{sky}(\nu; \theta') + T_{\parallel}^{gnd}(\theta') \\ T_{b\perp}(\nu; \theta') &= T_{\perp}^{sky}(\nu; \theta') + T_{\perp}^{gnd}(\theta') \end{aligned} \quad (15)$$

$$\begin{aligned} T_{\parallel}^{sky}(\nu; \theta_1) &= \Gamma_{\parallel}(\theta_1) T_b^{sky}(\nu; \theta_1) & T_{\perp}^{sky}(\nu; \theta_1) &= \Gamma_{\perp}(\theta_1) T_b^{sky}(\nu; \theta_1) \\ T_{\parallel}^{gnd}(\theta_1) &= [1 - \Gamma_{\parallel}(\theta_1)] T_{gnd} & T_{\perp}^{gnd}(\theta_1) &= [1 - \Gamma_{\perp}(\theta_1)] T_{gnd} \end{aligned} \quad (16)$$

$$\begin{aligned}\Gamma_{\parallel}(\theta_1) &= \left| \frac{\cos \theta_1 - \sqrt{\varepsilon_2 - \sin^2 \theta_1}}{\cos \theta_1 + \sqrt{\varepsilon_2 - \sin^2 \theta_1}} \right|^2 \\ \Gamma_{\perp}(\theta_1) &= \left| \frac{\varepsilon_2 \cos \theta_1 - \sqrt{\varepsilon_2 - \sin^2 \theta_1}}{\varepsilon_2 \cos \theta_1 + \sqrt{\varepsilon_2 - \sin^2 \theta_1}} \right|^2\end{aligned}\quad (17)$$

where  $T_{gnd}$  and  $\varepsilon_2$  are, respectively, the ground temperature and its relative permittivity,  $\theta_1 = \pi - \theta'$  and  $\Gamma_{\parallel}(\theta_1)$  and  $\Gamma_{\perp}(\theta_1)$  indicate the power reflection coefficients at the ground-air interface. The relation between  $(\theta, \phi)$  and  $(\theta', \phi')$  is still described by (3). Since the emission and scattering from ground is a polarization dependent process, the polarization components,  $\parallel$  and  $\perp$ , are introduced. Finally,  $P_{\parallel}$  and  $P_{\perp}$  are respectively the horizontal and vertical power pattern components in the incident plane of the ground-air interface. According to what reported in section 2, it results that  $P_{\parallel} \equiv P_{\theta'}$  and  $P_{\perp} \equiv P_{\phi'}$ .

The argument of the integral becomes (this will be further called ‘‘rigorous formula’’):

$$T_b(\nu; \theta', \phi') P_n(\nu; \theta, \phi) = \begin{cases} P_n(\nu; \theta, \phi) T_b^{sky}(\nu; \theta') & 0^\circ \leq \theta' \leq 90^\circ \\ P_{\parallel}(\nu; \theta, \phi) \left[ (1 - \Gamma_{\parallel}(\theta_1)) T_{gnd} + \Gamma_{\parallel}(\theta_1) T_b^{sky}(\theta_1) \right] + \\ + P_{\perp}(\nu; \theta, \phi) \left[ (1 - \Gamma_{\perp}(\theta_1)) T_{gnd} + \Gamma_{\perp}(\theta_1) T_b^{sky}(\theta_1) \right] & 90^\circ < \theta' \leq 180^\circ \end{cases} \quad (18)$$

Under certain conditions, i.e. assuming:

- i) unpolarized sources;
- ii) dry land,  $\varepsilon_2 \approx 3.5$ :  $\Gamma_{\perp}$  and  $\Gamma_{\parallel}$  are not very different from each other;
- iii) far-side lobes of the co-polar radiation pattern are very low compared with the maximum (i.e., approximately  $-40$ dB down) and comparable in value to the cross-polar pattern;
- iv) the antenna is not pointing to the ground;

it is possible to define an average reflection coefficient:

$$\bar{\Gamma}(\theta_1) = \frac{\Gamma_{\parallel}(\theta_1) + \Gamma_{\perp}(\theta_1)}{2} \quad (19)$$

Therefore (18) may be written as (“simplified formula”):

$$T_b(\nu; \theta', \phi') P_n(\nu; \theta, \phi) = \begin{cases} P_n(\nu; \theta, \phi) T_b^{sky}(\nu; \theta') & 0^\circ \leq \theta' \leq 90^\circ \\ P_n(\nu; \theta, \phi) [(1 - \bar{\Gamma}(\theta_1)) T_{gnd} + \bar{\Gamma}(\theta_1) T_b^{sky}(\theta_1)] & 90^\circ < \theta' \leq 180^\circ \end{cases} \quad (20)$$

Equation (20) is an estimation of the ground emission and scattering.

We have shown that in order to calculate the antenna temperature is necessary the knowledge of the power reflection coefficients that multiply the total power pattern ( $P_n$ ) (see (20)) or its perpendicular ( $P_{\perp}$ ) and parallel ( $P_{\parallel}$ ) components (see (18)). To avoid the calculation of the power reflection coefficients, a very-simplified formula is now introduced. In this new formula, the ground has been considered a black body (i.e. it doesn't reflect the incident fields directed on it). The very-simplified formula can be obtained by (20) where  $\bar{\Gamma}(\theta_1) = 0$ :

$$T_b(\nu; \theta', \phi') P_n(\nu; \theta, \phi) = \begin{cases} P_n(\nu; \theta, \phi) T_b^{sky}(\nu; \theta') & 0^\circ \leq \theta' \leq 90^\circ \\ P_n(\nu; \theta, \phi) T_{gnd} & 90^\circ < \theta' \leq 180^\circ \end{cases} \quad (21)$$

To better understand the effect of the power reflection coefficients we have used the Matlab script to calculate the factors which multiply the power pattern in (18), (20) and (21) at the frequency of 408MHz, at the same conditions suggested in [2]:  $\beta = 2.75$ ,  $T_{g_o} = 20$  K,  $\epsilon_2 \approx 3.5$  and  $T_{gnd} = 300$  K.

The results are reported in Fig.7: the black solid trace is equal to  $T_b^{sky}$  and this one, for  $0^\circ \leq \theta' \leq 90^\circ$ , is the unique factor for all the equations (18), (20) and (21).

On the other hand, for  $\theta' > 90^\circ$  the factors are different according to which power pattern components they come to multiply in the expressions,  $P_\perp$ , blue dashed trace, or  $P_\parallel$ , green dashed and dotted trace, for the rigorous one (18),  $P_n$  for the reduced one (20), red trace, or for the very-simplified one (21), pink with square marker trace.

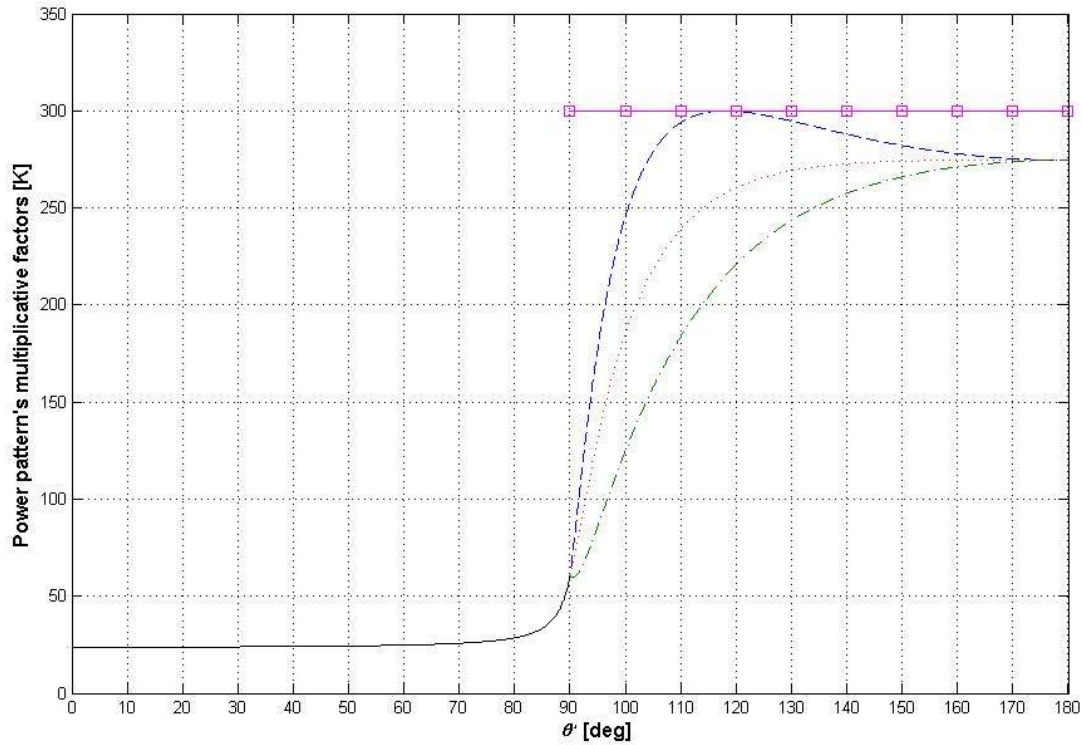


**Figure 7** – Dependence of the power pattern's multiplicative factor from its polarization and from the zenith angle for (18), (20) and (21).

#### 4. ALGORITHM DESCRIPTION

In this section, a complete description of the algorithm is carried out. The procedure consists of two main parts: in the first one, the antenna pattern needs to be evaluated through particular reflector antenna analysis tools (GRASP in our case). In the second part, a Fortran (or Matlab) code is used so performing an integral computation. In Fig.8, the algorithm flow-chart is sketched.

We have chosen to develop the code in Fortran and in Matlab for two main reasons:

- i) Matlab is an open source software, more friendly which allows to create suitable graphical interface (see Fig.9);
- ii) Fortran is more powerful and yields a relevant saving in the computation time (this point will be put in evidence in the section 6 with a comparison of the computation times for the two codes running in the same PC).

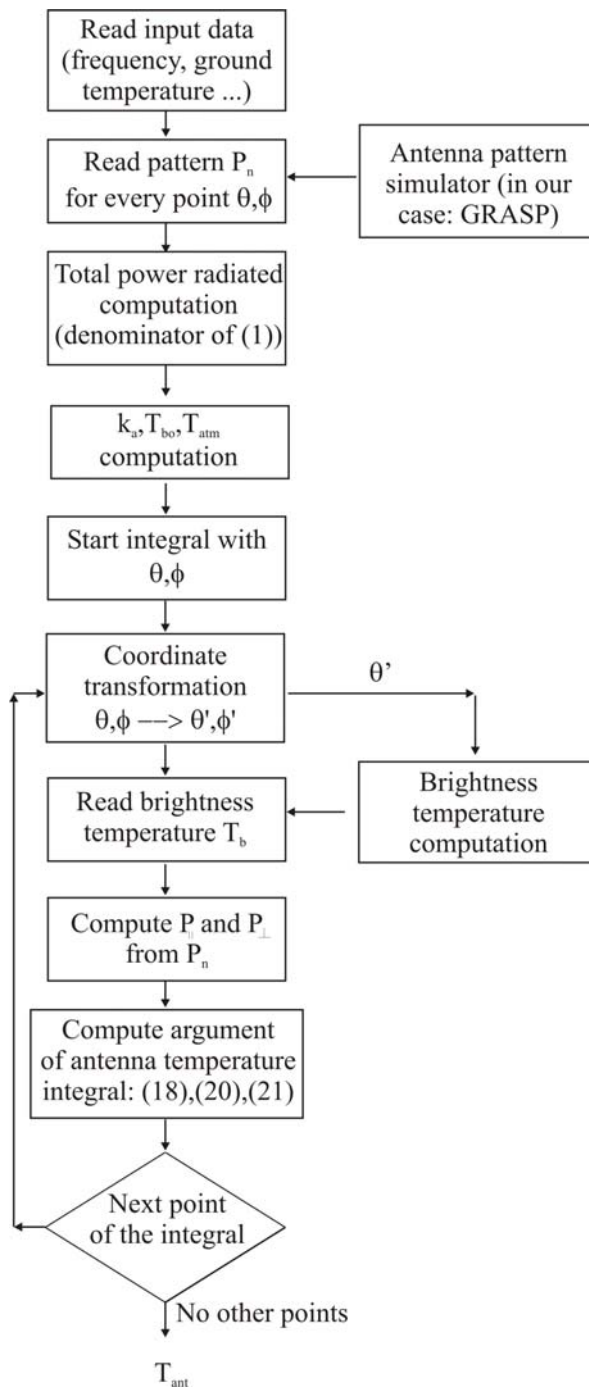


**Figure 8** – Algorithm flow-chart.

Input parameters for the Antenna Temperature c...

Frequency at which execute the calculations [GHz]:  
1

Ground temperature [K]:  
300

Spectral index:  
2.75

Base temperature for the Galactic emission calculation [K]:  
20

Relative permittivity of the ground  
3.5

Rotation angle of the antenna system around its main axis, Delta0 [deg]  
-90

Azimuth angle of the antenna axis, Phi0 [deg]  
90

Co-elevation angle, Theta0 [deg]  
45

OK Cancel

**Figure 9** – Input parameters windows in the Matlab code version.

## 5. BEST-1 DESCRIPTION

The BEST-1 test bed is based on a single N/S 7.5 x 23.5 m cylindrical-parabolic reflector as shown in Fig.10-a. Many information about BEST-1 can be found in [9,10] and at <http://www.ira.cnr.it/%7Eskawork>. The reflecting surface is made up of parallel steel wires located about 2 cm apart. The feed is positioned at the focal line and consists of 64  $\lambda/2$  dipoles, allowing a bandwidth of about 16MHz@408MHz ( $\lambda=0.735\text{m}$ ). In order, to concentrate the radiation pattern of the dipoles towards the cylindrical reflector, a flat sub-reflector is placed behind them, realised in practice by two contiguous structures: a small set of parallel steel wires and the aluminium ground plane of the dipoles' feed transmission lines (see Fig.10-b). Of course the antenna accepts just one single linear polarization. Four receivers, one every 16 dipoles (see Fig.10-c) have been installed on the focal line.

Via optical fiber links the amplified RF signals are sent to the receiver room located inside the central building, where they are converted to the intermediate frequency (30MHz). At this stage the

signals are summed up together after crossing analog phase shifters (digital phase shifter and beam-forming are planned to be used in the future), to form the total beam pattern. The beam pointing at the sky can take place in the following ranges: co-elevation  $-45^\circ \leq \theta' \leq 45^\circ$  with respect to the zenith direction (mechanical pointing) and right ascension  $-3.45^\circ \leq \alpha \leq 3.45^\circ$  with respect to the local meridian (electrical pointing).

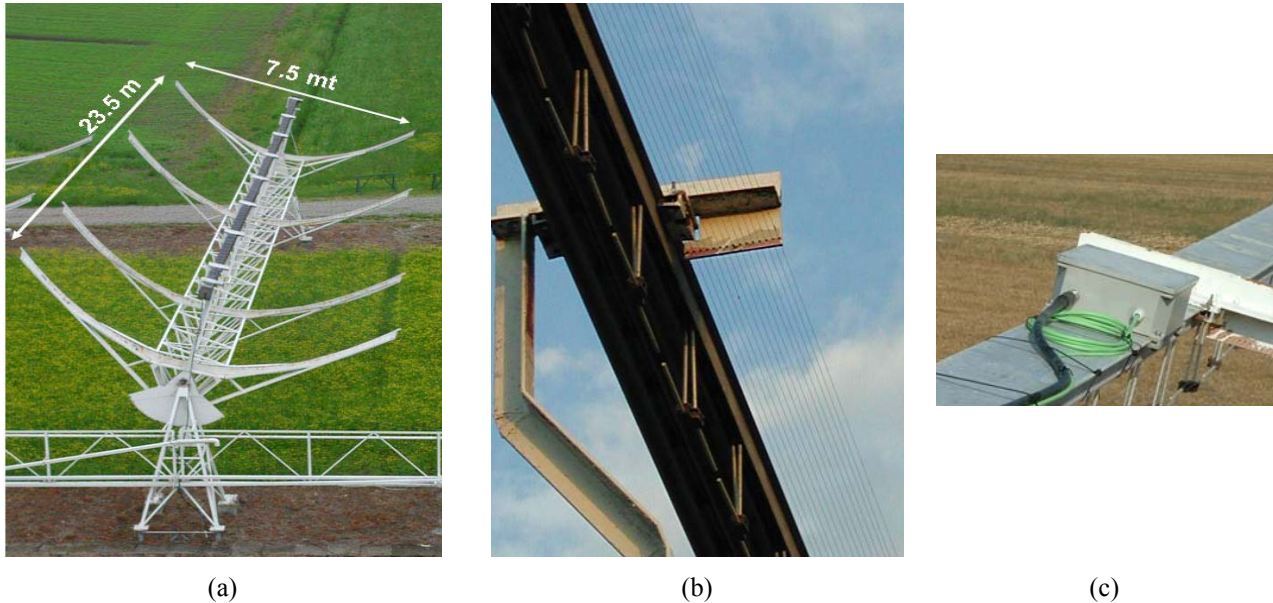


**Figure 10** - (a) N/S arm single cylinder (BEST-1), (b) dipole line feed with the hybrid subreflector and (c), one of four receivers installed on the focal line.

## 6. BEST-1 ELECTROMAGNETIC ANALYSIS & ANTENNA TEMPERATURE CALCULATION

In order to evaluate the antenna temperature of BEST-1, an electromagnetic analysis of this system has been performed; the study has been conducted through the commercial software GRASP developed by TICRA ([www.ticra.com](http://www.ticra.com)), which is based on the high frequency technique: Physical Optics (PO). GRASP is a very powerful and versatile tool to simulate and to design reflector antennas. Two reflectors compose the model introduced in GRASP to characterize BEST-1: a primary reflector and a sub-reflector. Due to the difficulty to describe within GRASP, structures with complex geometry, a rectangular plate is used to simulate the sub-reflector. Actually, as shown in Fig.10-b, the hybrid subreflector is more complex, but, as shown later, this assumption is confirmed by the results obtained.

The coordinate system of the antenna is located in the primary vertex and it is oriented as follows:

- x-axis along the parabolic profile of the mirror;
- y-axis along its cylindrical profile;
- z-axis along the forward direction of the antenna.

The antenna can rotate around the y-axis; since the antenna has just one degree of freedom, two of the three angles introduced in the section 2 are constant and equal to:  $\Delta_0 = -90^\circ$  and  $\Phi_0 = 90^\circ$ . The Fig.11 can help to better understand the procedure to rotate the antenna. These values simplify the formula to transform the reference systems.

The geometrical features of the two mirrors models are listed in the following (see also the model sketched in Fig.12).

For the primary mirror:

- total length along y-direction equal to 23.5m;
- total length along x-direction equal to 7.5m;
- focal length equal to 1.875m;
- the mirror, as already mentioned is not filled but rather composed by 0.5mm diameter steel wires spaced 2cm.

And about the sub-reflector:

- total length along y-direction equal to 23.5m;
- total length along x-direction equal to 0.374m;
- distance from the parabola vertex equal to 1.967m;
- the mirror is filled.

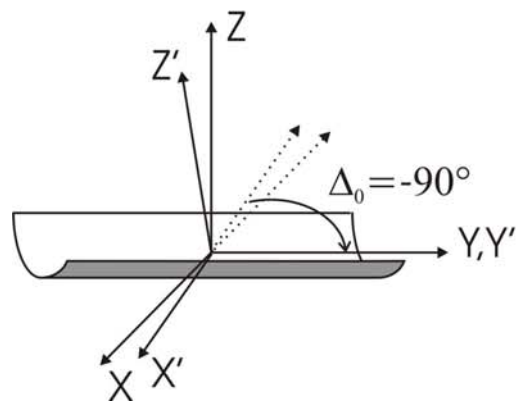
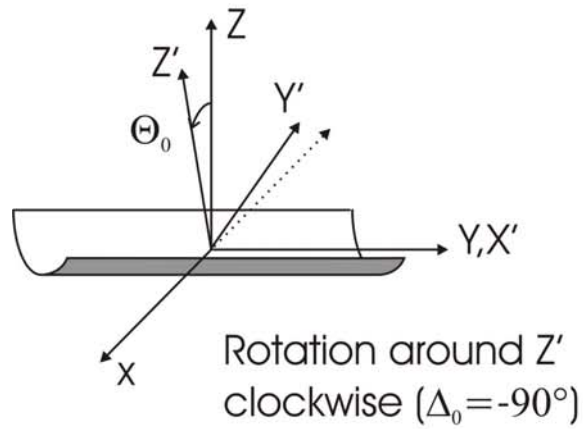
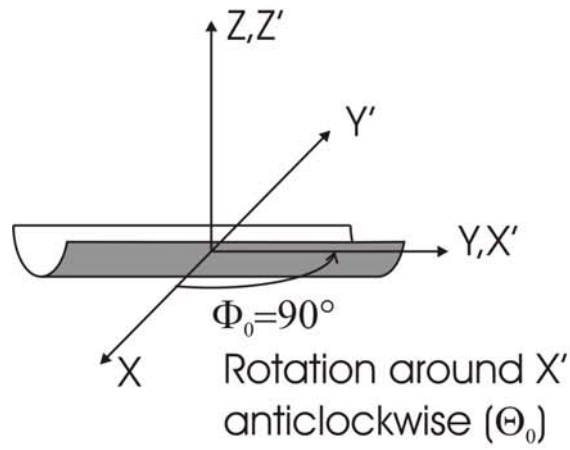
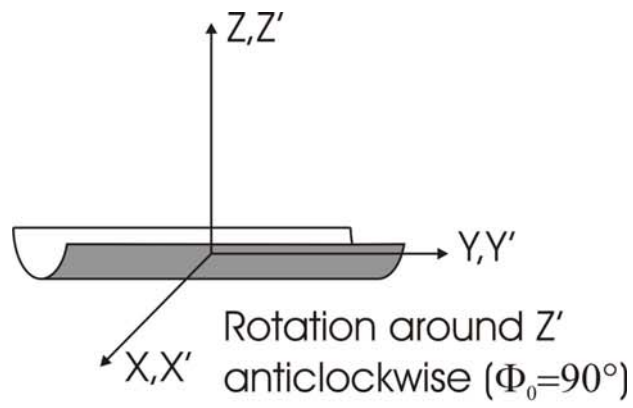


**Figure 11** – Rotation of coordinates  $x$ - $y$ - $z$  and  $x'$ - $y'$ - $z'$ .

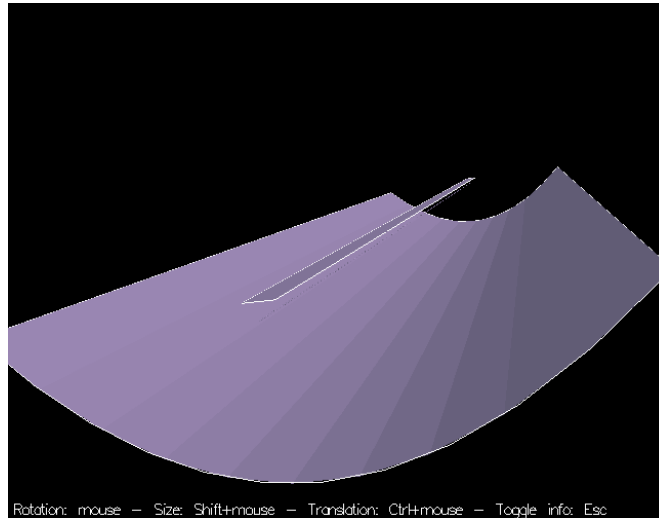


**Figure 12** – Geometrical model of BEST-1.

In the simulation, the four receivers illuminate the reflectors. All the receivers are fed with identical phase and amplitude. Hence, the feeding line is composed of 64  $\lambda/2$  dipoles aligned along the y-axis, spaced  $\lambda/2$  from each other. Moreover, the feeding line is  $\lambda/8$  far away from the focal line, closer to the parabola (distance from parabola vertex equal to 1.783m). The sub-reflector is  $\lambda/8$  shifted in the other direction. This configuration assumes that the illuminator (sub-reflector + feeding line) has a phase center half way between the two elements.

The aim of the electromagnetic analysis discussed in this report is to gather the knowledge of the power pattern in the whole space surrounding the structure. For a general study of the electromagnetic performance of BEST-1, we suggest to see [11]. It may help to recall that all the simulations in this section are carried out at 408MHz.

The whole system has been analyzed with PO: the idea is that the array feeds the sub-reflector inducing there a set of currents (PO\_secondary); then both the array and the sub-reflector feed the primary reflector (PO\_primary). Then, to take into account blockage effect, other currents (PO\_secondary#2) are induced in sub-reflector from scattering of the primary mirror. Finally, these four sources scatter a pattern in the far-field. The list of commands is:

1. PO\_secondary  $\leftarrow$  get currents  $\leftarrow$  Array
2. PO\_primary  $\leftarrow$  get composite currents  $\leftarrow$  PO\_secondary & array
3. PO\_secondary#2  $\leftarrow$  get currents  $\leftarrow$  PO\_primary
4. Spherical\_cut  $\leftarrow$  get fields  $\leftarrow$  Array
5. Spherical\_cut  $\leftarrow$  add fields  $\leftarrow$  PO\_primary
6. Spherical\_cut  $\leftarrow$  add fields  $\leftarrow$  PO\_secondary
7. Spherical\_cut  $\leftarrow$  add fields  $\leftarrow$  PO\_secondary#2

The evaluation of the pattern in all directions (even in the back lobe direction) yields a high number of points where the PO currents have to be sampled. The automatic convergence procedure suggests the PO1 and PO2 values reported in Table I. Additional investigations have been performed introducing in the currents computation even the Physical Theory of Diffraction, but no differences have been noticed.

	PO1	PO2
PO_secondary	1100	100
PO_secondary#2	100	13
PO_primary	32	105

**Table I** – POs number for GRASP computation.

Cylindrical antennas are characterized by different patterns in E-plane ( $\phi = 90^\circ$ ) and H-plane ( $\phi = 0^\circ$ ); hence, the patterns need to be evaluated in several azimuth cuts. Since the procedure to compute antenna temperature is very computer demanding, much attention has been devoted to investigate on the lowest possible points number in the field storage. The particular symmetry of the antenna allows saving from the electromagnetic computation several azimuthal cuts; in fact, every azimuth cut can be known with proper relations from the cuts in the  $(0^\circ-90^\circ)\phi$ -range. According to [12], the power pattern in each azimuth cut has been evaluated with a fine step in the main-lobe direction,  $(0^\circ-10^\circ)\theta$ -range, and with a rough step in all the other directions,  $(10^\circ-180^\circ)\theta$ -range.

In Table II, different values (according to (18)) of the antenna temperature at  $45^\circ$  zenith angle, are reported changing the number of the observation points for the scattered field. This iterative series of different simulation has assured the convergence of the antenna temperature integral.

As a conclusion of the values reported in Table II, we have verified that 91 azimuth planes (spaced each other of  $1^\circ$ ) and, for each azimuth cut, 251+251 points in the two  $\theta$ -ranges (i.e.  $0.04^\circ$  in the  $(0^\circ-10^\circ)\theta$ -range and  $0.68^\circ$  in the  $(10^\circ-180^\circ)\theta$ -range) are adequate. This sampling yields to a dimension of each storage file of about 1.675Mbyte.

<b>Azimuth planes in (0°-90°) <math>\phi</math>-range</b>	<b>Elevation points in (0°-10°) + (10°-180°) <math>\theta</math>-ranges</b>	<b>PTD</b>	<b>Antenna temperature [K]</b>
46 ( $d\phi = 2^\circ$ )	1001+1001 ( $d\theta = 0.01^\circ; d\theta = 0.17^\circ$ )	No	52.9
46 ( $d\phi = 2^\circ$ )	501+501 ( $d\theta = 0.02^\circ; d\theta = 0.34^\circ$ )	No	52.9
<b>91 (<math>d\phi = 1^\circ</math>)</b>	<b>251+251</b> ( $d\theta = 0.04^\circ; d\theta = 0.68^\circ$ )	<b>No</b>	<b>51.0</b>
91 ( $d\phi = 1^\circ$ )	251+251 ( $d\theta = 0.04^\circ; d\theta = 0.68^\circ$ )	Yes	51.2
181 ( $d\phi = 0.5^\circ$ )	251+251 ( $d\theta = 0.04^\circ; d\theta = 0.68^\circ$ )	No	51.0

**Table II** – Observation point numbers for antenna temperature computation. The values in row 3 are the ones that we have chosen.

In order to verify the correct results of the GRASP simulation, the directivity is computed and used to compare results with those reported in [11]. The maximum directivity ( $D_0$ ) is equal to 34.6dB, corresponding to an effective area of:

$$A_{eff} = \frac{D_0 \lambda^2}{4\pi} = 124.69m^2$$

Since the geometrical area of the antenna ( $A_{geo}$ ) is  $176.25m^2$ , the antenna efficiency is:

$$\epsilon_{ant} = \frac{A_{eff}}{A_{geo}} = 0.71$$

This value has to be confronted with the figure 0.74, estimated in [11]. If we consider that the EM procedure to study the antenna is based: in this report on the PO technique, whereas in [11] on the solution of the Pocklington equation through a bi-dimensional Method of Moment, we can consider with satisfaction the agreement between the two cited values.

In Fig.13, a bi-dimensional grid of the antenna pattern in the  $uv$ -plane is plotted near the main beam; as expected, the rectangular shape of the aperture yields a fan beam where the main axis is in H-plane and the minor axis in the E-plane.

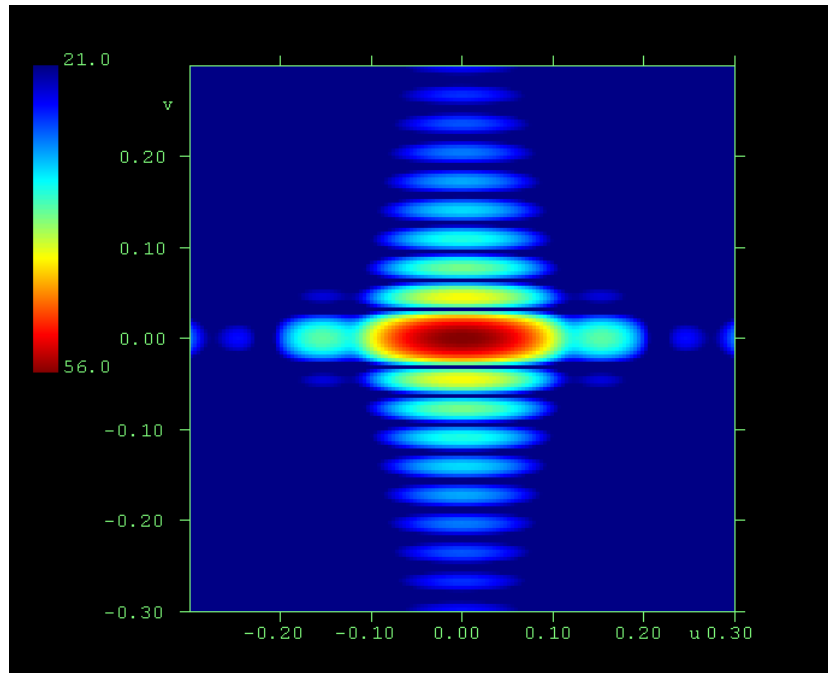


**Figure 13** – Antenna 2-D beam.

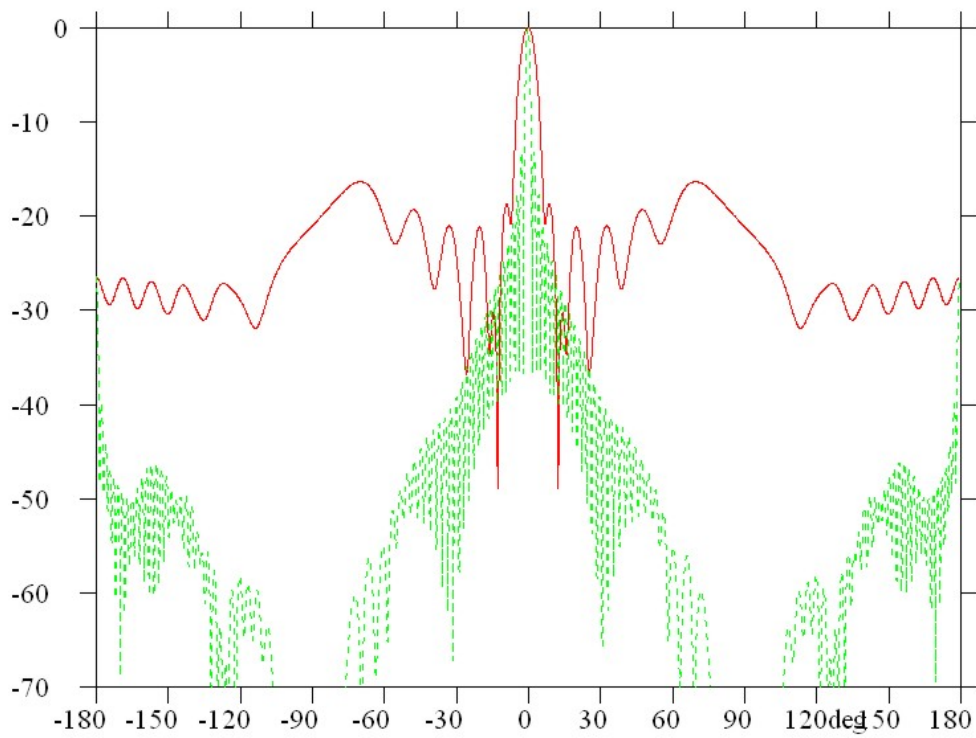


**Figure 14** – Normalized power pattern in E-plane (dashed, green curve) and in the H-plane (continued, red curve).

As mentioned already, in order to compute the antenna temperature, the pattern has to be computed in the whole space surrounding the antenna. In Fig.14, the antenna pattern is plotted in the two main planes. The inter-distance between elements is less than  $\lambda/2$ , so grating lobes are avoided. As shown, the beam in the E-plane is narrower than that in the H-plane. It is interesting to plot the power radiated from the antenna in every azimuth cuts (Fig.15), where one can appreciate that the majority of the power scattered by BEST-1 is concentrate in the H-plane.

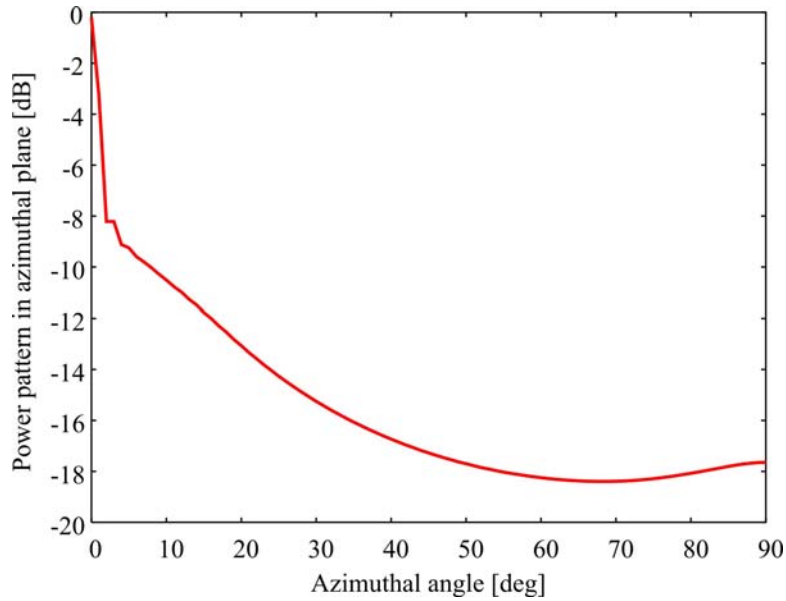


**Figure 15** – Power radiated in azimuthal cuts

At this point, it is possible to compute the antenna temperature at different pointing elevations of the antenna. Concerning to the galactic contribution, the average value  $T_{g_o} = 20$  K (see (11)) has been used [2]. In Fig.16, the antenna temperature is plotted against zenith angles. Notwithstanding the maximum co-elevation is  $45^\circ$ , the numerical analysis has been expanded up to  $80^\circ$ , this allows us to have a more general view of the antenna temperature behavior. In detail, ten different points are considered between zenith  $\Theta_0 = 0^\circ$  and quasi-horizon  $\Theta_0 = 80^\circ$ . The three curves are related to the contributions coming from the ground ( $\theta' > 90^\circ$ ) and from the sky ( $\theta' \leq 90^\circ$ ). Finally, the red cross curve shows the total antenna temperature sum of the previous two contributions. This computation has been done according to the rigorous equation (18). Just a few comments on these curves: the contribution from the sky is almost constant at any pointing direction, depending basically from what the antenna gets through its main beam (we have seen that at 408MHz, the brightness temperature is not very fluctuating with the zenithal angle: 23.8K at zenith and 28.5K at

80°). As far as the ground contribution is concerned, the temperature increases when antenna goes down because, according to expectations, the side lobes point now versus the hot ground.

In order to verify these numerical results with some historical experimental measurements we have looked in former technical reports. In these reports different antenna temperatures without dependence with the antenna pointing angle were evaluated for the E/W arm. Obviously, we can assume that these values don't change considerably for the N/S arm. In 1977 the antenna temperature was estimated to be 40K, [13], and in 1992 to be 30K, [14]. Anyway, both these values agree with the 35K found from our numerical results for the zenith direction.

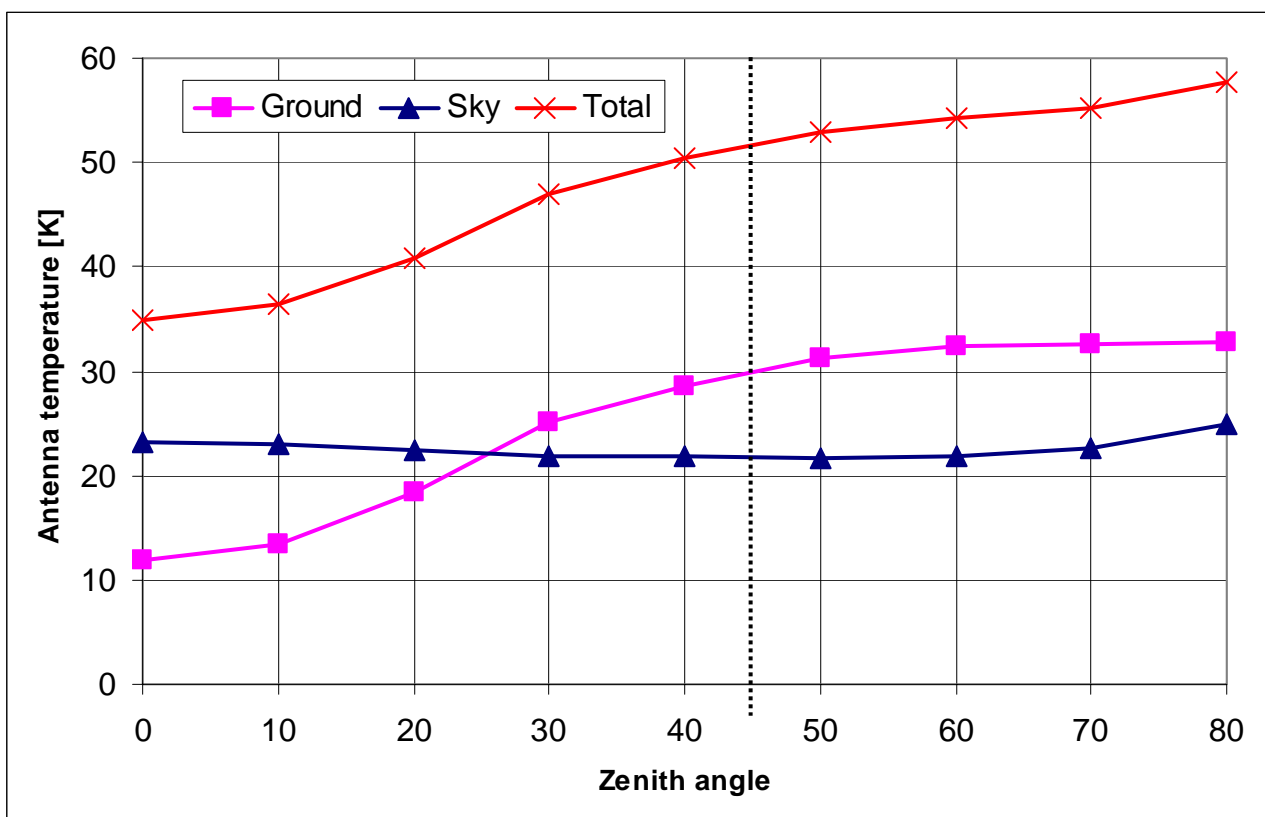


Figure 16 – Antenna temperature contributions against zenith angle.

It is worth noticing the good agreement among the very-simplified formula, (21), the simplified one, (20), and the rigorous one, (18) as shown in Fig.17, where the curves representing the antenna temperature evaluated by the three formulas show a similar behavior. Only a sheer of few Kelvin degrees difference is noted. The difference between the three formulas increases with the zenith angle; this confirms the condition of validity of (20) and consequently of (21), as deeply discussed

in section 3 and in [2]. However, it is important to note that both the very-simplified and the simplified formulas don't allow a time saving in the antenna temperature calculation. Hence, a recommendation to use the rigorous formula is given. On the other hand, simplified formula could be chosen when antenna pattern is known in terms of total power pattern and it is not possible to get the linear, parallel and perpendicular, components which are necessary to perform the rigorous formula. Moreover, when it isn't possible to know neither the power reflection coefficients (21) should be used.

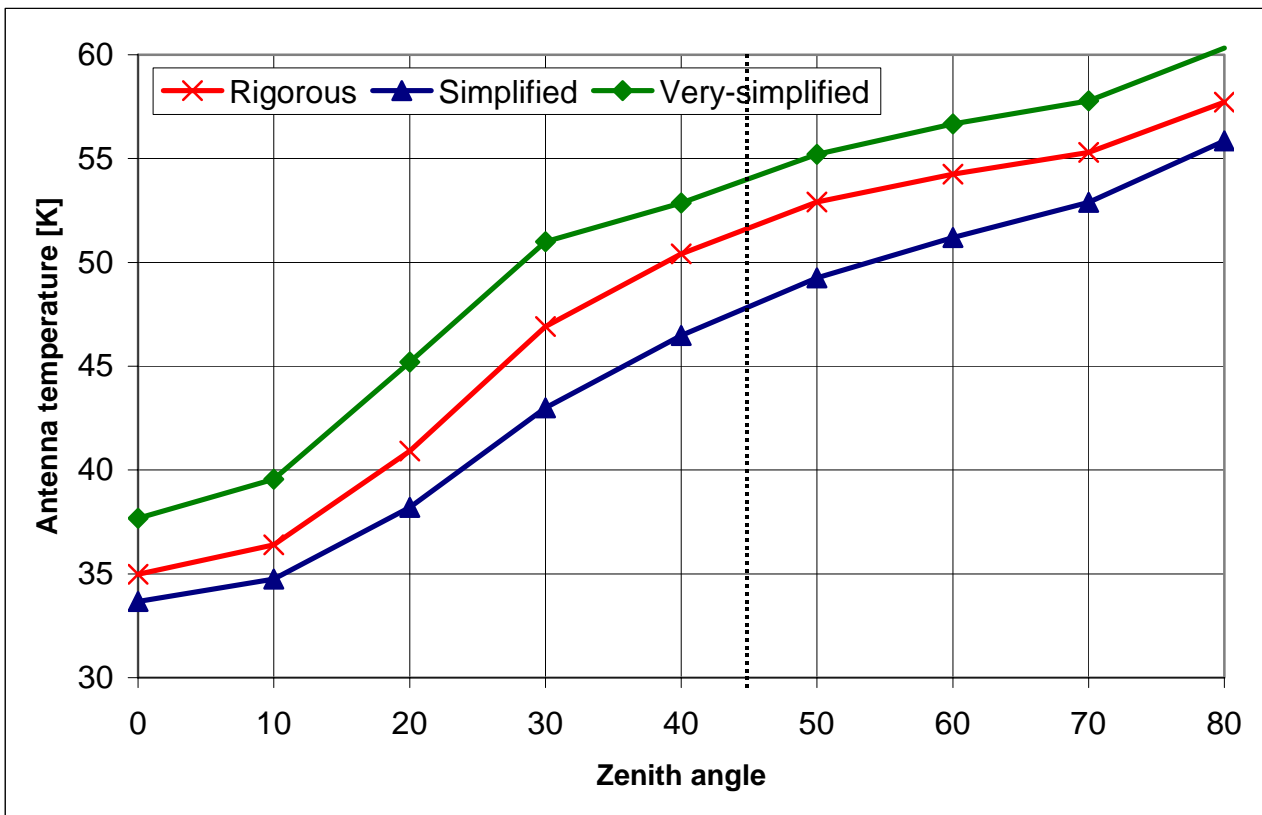


Figure 17 – Antenna temperature against zenith angle.

In the Fig.18, we'd like to show the strong dependence of the antenna temperature to the galactic temperature: this happens at low frequencies, as 408MHz. According to [2], three different values of  $T_{g_0}$  have been used: 3K (very close to the cosmic microwave background), 20K (average value) and 507K (galactic centre). Actually, these galactic temperatures are located in regions of sky not visible from Medicina with BEST: for example the galactic centre is below the horizon of Medicina. Anyway, exploring the 408MHz map reported in [3], we have found that very similar values can be get also from Medicina.

The total PC time computation (Pentium Athlon XP - 2.2GHz – 512MB RAM) to compute the antenna temperature integral for each pointing elevation angle is the following: 50 minutes and 150 minutes, respectively for the Fortran and the Matlab version. As expected, the Fortran version is faster than the Matlab one.

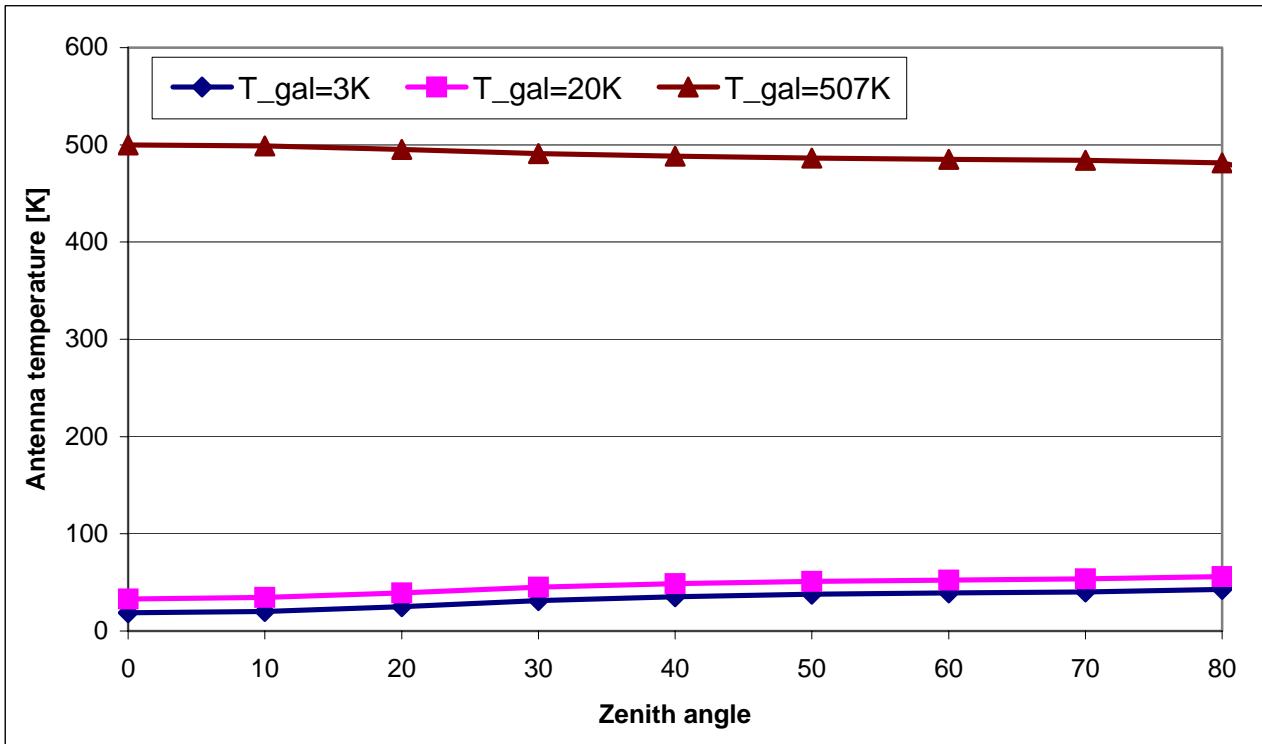


Figure 18 – Antenna temperature against zenith angle for different galactic temperatures.

## 7. ACKNOWLEDGMENT

The authors are grateful to Dr. Goliardo Tomassetti and Eng. Germano Bianchi, reviewers of this report. GRASP commercial software is licensed at Computational Electromagnetic Lab of the University of Florence.

## 8. REFERENCES

- [1] J. Dijk, H.H.H. Groothuis, E.J. Maanders, "Some improvements in antenna noise temperature calculation," *IEEE Trans. Ant. Propagat.*, September 1970, pp. 690-692.
- [2] G. Cortes Medellin, "Antenna Noise Temperature Calculations," *SKA Technical Memo Series*, October 20, 2004.
- [3] G. Giardino, *et al.*, "Towards a model of full-sky Galactic synchrotron intensity and linear polarization: A re-analysis of the Parkes data," *Astronomy and Astrophysics*, Vol. 387, pp. 82-97, 2002.
- [4] C.G.T. Haslam, *et al.*, "A 408 MHz all-sky continuum survey," *Astronomy and Astrophysics Supplement Series*, Vol. 47, pp. 1-143, Jan. 1982.
- [5] Yogg Han and Ed R. Westwater, "Analysis and Improvement of Tipping Calibration for Ground-Based Microwave Radiometers", *IEEE Transaction on Geoscience and Remote Sensing*, Vol 38, No. 3, May 2000.
- [6] Matlab help, function trapz.
- [7] W.J. Palm III, "Matlab 6 per l'ingegneria e le scienze", McGraw-Hill, 2001.
- [8] G. Brussaard, P.A. Watson, "Atmospheric modeling and millimeter wave propagation", Chapman&Hall, 1995.
- [9] S. Montebugnoli, *et al.*, "Re-instrumentation of the Northern Cross Radio Telescope for a SKA cylindrical concentrator based test bed", *IEE Conference Proceeding*, Vol. 3, pp. 1537-1540, 2004.
- [10] S. Montebugnoli, *et al.*, "Large antenna array remoting using Radio-over-Fiber techniques for radio astronomical application", *Microwave and Optical technology letters*, Vol. 46, 2005.
- [11] G. Virone, R. Tascone, O.A. Peverini, M. Baralis, A. Olivieri, "Analisi della antenne a riflettore che compongono il ramo Nord-Sud della Croce del Nord," *Rapporto tecnico EA/031125*.
- [12] C. Allen, "Parametric analysis of Cassegrain antenna noise temperature by numerical methods," *Antennas and Propagation Society International Symposium*, 1971, Vol. 9, Sept. 1971, pp. 212-215.
- [13] R. Ambrosini, G. Tomassetti, "Proposta per il Raddoppio della Sensibilità del Ramo E-W della Croce del Nord," *Rapporto tecnico IRA 21/77*, 1977.
- [14] C. Bortolotti, S. Montebugnoli, G. Tomassetti, "Miglioramento della sensibilità del ramo E/W della Croce del Nord: Installazione di 12 preamplificatori a GaAs Fet distribuiti lungo l'antenna," *Rapporto tecnico IRA 172/92*, 1992.

## APPENDIX A

**Table A-1** - Tabulated Sky Brightness Temperature for different zenith angles

Freq	$T_b^{sky}(0^\circ)$	$T_b^{sky}(60^\circ)$	$T_b^{sky}(85^\circ)$	$T_b^{sky}(90^\circ)$
[GHz]	[K]	[K]	[K]	[K]
0.02	7.99E+04	7.99E+04	7.98E+04	7.98E+04
0.03	2.62E+04	2.62E+04	2.62E+04	2.61E+04
0.04	1.19E+04	1.19E+04	1.19E+04	1.18E+04
0.05	6.43E+03	6.43E+03	6.41E+03	6.38E+03
0.06	3.90E+03	3.89E+03	3.88E+03	3.86E+03
0.07	2.55E+03	2.55E+03	2.54E+03	2.52E+03
0.08	1.77E+03	1.77E+03	1.76E+03	1.74E+03
0.09	1.28E+03	1.28E+03	1.27E+03	1.26E+03
0.1	9.58E+02	9.57E+02	9.52E+02	9.41E+02
0.2	1.45E+02	1.45E+02	1.47E+02	1.53E+02
0.3	5.00E+01	5.07E+01	5.66E+01	7.43E+01
0.4	2.49E+01	2.59E+01	3.43E+01	6.09E+01
0.5	1.54E+01	1.66E+01	2.68E+01	5.99E+01
0.6	1.10E+01	1.24E+01	2.38E+01	6.18E+01
0.7	8.75E+00	1.02E+01	2.25E+01	6.40E+01
0.8	7.43E+00	8.98E+00	2.19E+01	6.61E+01
0.9	6.62E+00	8.22E+00	2.16E+01	6.79E+01
1	6.10E+00	7.74E+00	2.15E+01	6.94E+01
1.2	5.49E+00	7.20E+00	2.15E+01	7.18E+01
1.4	5.18E+00	6.93E+00	2.16E+01	7.34E+01
1.6	5.00E+00	6.79E+00	2.17E+01	7.47E+01
1.8	4.90E+00	6.71E+00	2.19E+01	7.58E+01
2	4.83E+00	6.66E+00	2.20E+01	7.67E+01
3	4.74E+00	6.65E+00	2.26E+01	8.04E+01
4	4.77E+00	6.76E+00	2.34E+01	8.43E+01
5	4.85E+00	6.93E+00	2.43E+01	8.89E+01
6	4.95E+00	7.14E+00	2.55E+01	9.43E+01
7	5.08E+00	7.40E+00	2.68E+01	1.01E+02
8	5.24E+00	7.72E+00	2.85E+01	1.08E+02
9	5.43E+00	8.10E+00	3.04E+01	1.17E+02
10	5.66E+00	8.55E+00	3.27E+01	1.26E+02
12	6.26E+00	9.74E+00	3.86E+01	1.50E+02
14	7.17E+00	1.15E+01	4.73E+01	1.79E+02
16	8.71E+00	1.45E+01	6.15E+01	2.17E+02
18	1.18E+01	2.05E+01	8.76E+01	2.59E+02
20	1.92E+01	3.46E+01	1.39E+02	2.88E+02
21	2.56E+01	4.66E+01	1.74E+02	2.93E+02
22	3.14E+01	5.70E+01	1.97E+02	2.94E+02
23	2.95E+01	5.37E+01	1.90E+02	2.94E+02
24	2.41E+01	4.39E+01	1.66E+02	2.92E+02
25	2.00E+01	3.61E+01	1.44E+02	2.89E+02
26	1.75E+01	3.14E+01	1.28E+02	2.84E+02
27	1.60E+01	2.87E+01	1.19E+02	2.80E+02
28	1.53E+01	2.73E+01	1.14E+02	2.77E+02
29	1.51E+01	2.69E+01	1.12E+02	2.75E+02
30	1.51E+01	2.70E+01	1.12E+02	2.74E+02

Freq	$T_b^{sky}(0^\circ)$	$T_b^{sky}(60^\circ)$	$T_b^{sky}(85^\circ)$	$T_b^{sky}(90^\circ)$
[GHz]	[K]	[K]	[K]	[K]
32	1.59E+01	2.84E+01	1.17E+02	2.75E+02
34	1.73E+01	3.10E+01	1.25E+02	2.79E+02
36	1.92E+01	3.47E+01	1.37E+02	2.83E+02
38	2.18E+01	3.96E+01	1.52E+02	2.87E+02
40	2.53E+01	4.60E+01	1.69E+02	2.90E+02
42	3.00E+01	5.45E+01	1.89E+02	2.92E+02
44	3.66E+01	6.62E+01	2.12E+02	2.93E+02
46	4.63E+01	8.29E+01	2.36E+02	2.94E+02
48	6.17E+01	1.08E+02	2.60E+02	2.95E+02
50	8.88E+01	1.48E+02	2.78E+02	2.95E+02
52	1.51E+02	2.19E+02	2.89E+02	2.95E+02
54	2.62E+02	2.83E+02	2.93E+02	2.95E+02
56	2.88E+02	2.92E+02	2.95E+02	2.95E+02
58	2.91E+02	2.93E+02	2.95E+02	2.95E+02
60	2.92E+02	2.94E+02	2.95E+02	2.95E+02
62	2.92E+02	2.93E+02	2.95E+02	2.95E+02
64	2.88E+02	2.92E+02	2.95E+02	2.95E+02
66	2.57E+02	2.82E+02	2.93E+02	2.95E+02
68	1.66E+02	2.33E+02	2.90E+02	2.95E+02
70	1.17E+02	1.84E+02	2.85E+02	2.95E+02
72	9.25E+01	1.53E+02	2.80E+02	2.95E+02
74	7.81E+01	1.33E+02	2.74E+02	2.95E+02
76	6.90E+01	1.19E+02	2.68E+02	2.95E+02
78	6.31E+01	1.10E+02	2.63E+02	2.95E+02
80	5.92E+01	1.04E+02	2.59E+02	2.95E+02
82	5.66E+01	1.00E+02	2.56E+02	2.95E+02
84	5.50E+01	9.73E+01	2.54E+02	2.95E+02
86	5.41E+01	9.58E+01	2.53E+02	2.95E+02
88	5.36E+01	9.52E+01	2.53E+02	2.95E+02
90	5.36E+01	9.51E+01	2.53E+02	2.95E+02
92	5.39E+01	9.57E+01	2.54E+02	2.95E+02
94	5.45E+01	9.66E+01	2.55E+02	2.95E+02
96	5.53E+01	9.80E+01	2.57E+02	2.95E+02
98	5.64E+01	9.97E+01	2.58E+02	2.95E+02
100	5.77E+01	1.02E+02	2.60E+02	2.95E+02